Editors' Suggestion

Interacting defects generate stochastic fluctuations in superconducting qubits

J. H. Béjanin, C. T. Earnest, A. S. Sharafeldin,* and M. Mariantoni†
Institute for Quantum Computing, University of Waterloo, 200 University Avenue West, Waterloo, Ontario, Canada N2L 3G1 and Department of Physics and Astronomy, University of Waterloo, 200 University Avenue West, Waterloo, Ontario, Canada N2L 3G1

(Received 29 June 2021; revised 18 August 2021; accepted 1 September 2021; published 21 September 2021)

Amorphous dielectric materials have been known to host two-level systems (TLSs) for more than four decades. Recent developments on superconducting resonators and qubits enable detailed studies on the physics of TLSs. In particular, measuring the loss of a device over long time periods (a few days) allows us to investigate stochastic fluctuations due to the interaction between TLSs. We measure the energy relaxation time of a frequency-tunable planar superconducting qubit over time and frequency. The experiments show a variety of stochastic patterns that we are able to explain by means of extensive simulations. The model used in our simulations assumes a qubit interacting with high-frequency TLSs, which, in turn, interact with thermally activated low-frequency TLSs. Our simulations match the experiments and suggest the density of low-frequency TLSs is about three orders of magnitude larger than that of high-frequency ones.

DOI: 10.1103/PhysRevB.104.094106

I. INTRODUCTION

Superconducting devices operated in the quantum regime [1] are ideal tools to study the properties of amorphous dielectric materials [2]. These materials are known to be characterized by defects that can be modeled as two-level systems (TLSs) [3]. TLSs can interact with superconducting resonators or qubits, resulting in dissipation channels that are particularly prominent in planar devices. Such devices are fabricated by depositing superconducting films made from metals, e.g., aluminum (Al) or niobium, on silicon (Si) or sapphire substrates. A few examples of planar devices can be found in our works of Refs. [4,5], where we have investigated coplanar waveguide (CPW) resonators [6] as well as Xmon transmon qubits [7].

A large body of work on CPW resonators and qubits has shown that TLSs are likely hosted in native oxide layers [8–17] at the substrate-metal (SM), substrate-air (SA), or metal-air (MA) interfaces [4,18–20]. TLSs originate within these layers because naturally occurring oxides deviate from crystalline order. This deviation may result in trapped charges, dangling bonds, tunneling atoms, or collective motion of molecules.

It is convenient to distinguish between two categories of TLSs based on their energy E and the device operating temperature T. When $E > k_B T$, the corresponding TLSs reside in the quantum ground state; these TLSs are hereafter referred to as quantum-TLSs (Q-TLSs). When $E < k_B T$, the TLSs are thermally activated and are referred to as thermal-TLSs (T-TLSs). Typically, superconducting resonators are characterized by a resonance frequency f_r and qubits by a transition frequency f_q, with $f_r \sim f_q \sim 5$ GHz, and are operated at $T \sim 50$ mK. Hence, the energy threshold between Q- and T-TLSs is $E/h \sim 1$ GHz.

Superconducting quantum devices interact (semi)resonantly with Q-TLSs [21], affecting the internal quality factor of resonators Q_i or the energy relaxation time of qubits T_1. Several authors have hypothesized that Q-TLSs additionally interact with T-TLSs [22–24], leading to experimentally observed stochastic fluctuations in Q_i and f_r [15,16,22,25] as well as T_1 and f_q [2,26]. The model proposed by these authors departs from the TLS standard tunneling model (STM), where TLS interactions are neglected [3]. The interacting model is sometimes called the *generalized tunneling model* (GTM).

It has recently been shown that planar fixed-frequency transmon qubits exhibit random fluctuations in both T_1 and f_q over very long time periods [27–29]. Frequency-tunable transmon qubits, as the Xmon, show TLS-induced fluctuations predominantly in T_1 [30]. TLS-induced f_q fluctuations are present but are overshadowed by additional noise processes such as flux noise.[1] These findings serve as the main motivation for the experiments and simulations presented in this paper.

In this paper, we present the experimental measurement of spectrotemporal charts for an Xmon transmon qubit as well as the results of detailed simulations corresponding to these experiments. In the spectrotemporal charts, T_1 is measured and simulated for time periods up to 48 h and for f_q ranges up to 300 MHz. Our main objective is to validate the Q-TLS–T-TLS interaction hypothesis in the GTM by comparing experiments and simulations. In our simulations, a qubit interacts with an ensemble of Q-TLSs, the frequencies of which undergo

*Present address: Department of Engineering Physics, McMaster University, Hamilton, Ontario, Canada L8S 4L7.
†Corresponding author: matteo.mariantoni@uwaterloo.ca

[1]The flux noise experienced by tunable transmon qubits is caused by the increased flux sensitivity due to the SQUID (see Appendix B).

stochastic fluctuations due to the interaction with T-TLSs. For every Q-TLS we consider a set of interacting T-TLSs, where the dynamics of each T-TLS state are governed by a random telegraph signal (RTS). The Q-TLS frequency fluctuation process, which is broadly referred to as *spectral diffusion*, is responsible for the random fluctuations in T_1.

The comparison between experiments and simulations reveals that the Q-TLS–T-TLS interaction likely exists, as proposed in the GTM. In particular, our simulations reproduce well the spectral-diffusion patterns presented in the experiments. Our model suggests that the density of T-TLSs is significantly higher than that of Q-TLSs. We find a T-TLS density of approximately $6 \times 10^5\,\mathrm{GHz}^{-1}\;\mu\mathrm{m}^{-3}$, which is about three orders of magnitude larger than the Q-TLS density.

Finally, we show that certain statistical analyses, such as the Allan deviation, are not able to capture the fluctuation characteristics of a given time series (e.g., the number of T-TLSs contributing to the stochastic process). Instead, a direct analysis of the time series provides a more accurate description of the stochastic processes due to TLSs.

The paper is organized as follows. In Sec. II, we review the theory necessary to describe the stochastic fluctuations of T_1. In Sec. III, we explain the methods required to perform experiments and simulations. In Sec. IV, we present our main results. In Sec. V, we provide an in-depth discussion on some of our main results. Finally, in Sec. VI, we summarize our findings and suggest a road map for future work.

II. THEORY

In this section, we introduce physical models of TLSs (Sec. II A); we then describe the qubit–Q-TLS and Q-TLS–T-TLS interaction (Secs. II B and II C); finally, we amalgamate the previous concepts in order to explain qubit stochastic fluctuations (Sec. II D).

A. Physical models of TLSs

The STM is a phenomenological model describing defects in amorphous dielectric materials. The defects are commonly assumed to be quantum-mechanical double-well potentials, or TLSs, with energy barrier V. In the STM, the TLS tunneling energy Δ_0 is calculated by means of the Wentzel-Kramers-Brillouin (WKB) approximation,

$$\Delta_0 \simeq h\Omega_0 \exp\left(-\frac{d}{\hbar}\sqrt{2\,mV}\right). \tag{1}$$

In this equation, Ω_0 is the attempt frequency (assumed to be the same for both wells), d is the spatial distance between the two wells, and m is the mass of the physical entity associated with the TLS (e.g., a molecular mass) [31].

The unperturbed Hamiltonian of a TLS reads as $\widehat{H}_{\mathrm{TLS}} = (\Delta\hat{\hat{\sigma}}_z + \Delta_0\hat{\hat{\sigma}}_x)/2$, where Δ is the asymmetry energy between the two wells of the TLS; $\hat{\hat{\sigma}}_z$ and $\hat{\hat{\sigma}}_x$ are the usual Pauli matrices in the so-called diabatic ("left" and "right") basis. By diagonalizing this Hamiltonian we obtain $\widehat{H}_{\mathrm{TLS}} = E\,\hat{\sigma}_z/2$, where

$$E = \sqrt{\Delta^2 + \Delta_0^2} \tag{2}$$

is the TLS energy and $\hat{\sigma}_z = [\hat{\hat{\sigma}}_z \cos(\theta) + \hat{\hat{\sigma}}_x \sin(\theta)]/2$ is the Pauli matrix in the energy basis; $\theta = \arctan(\Delta_0/\Delta)$ is the rotation angle used to perform the diagonalization.

One of the hypotheses in the STM is that Δ and Δ_0 are uncorrelated quantities with joint probability density

$$f_{\Delta,\Delta_0} = \begin{cases} \dfrac{D}{\Delta_0}, & \text{for } \Delta \geqslant 0 \text{ and } \Delta_0 \geqslant \mathcal{E}_{\min}; \\ 0, & \text{otherwise.} \end{cases} \tag{3}$$

In this equation, D is the TLS density in units of inverse energy and volume and $\mathcal{E}_{\min}$ is the minimum tunneling energy. A further hypothesis is that interactions between TLSs are very weak and, thus, *negligible*.

The hypotheses behind the STM prevent this model from explaining a variety of features observed in devices affected by TLS defects. Among other phenomena, the STM cannot explain the temperature dependence of the frequency noise of superconducting resonators [22] as well as the strong temperature dependence of the relaxation rate of Q-TLSs measured with qubits [32]. Most importantly, the STM cannot explain the spectral diffusion dynamics observed both in the work of Ref. [30] and in our experiments.

In order to resolve these shortcomings, it is necessary to extend the STM to the GTM by making the following modifications:

(1) Interactions between TLSs are not neglected.

(2) The joint probability density is assumed to be nonuniform with respect to Δ,

$$f_{\Delta,\Delta_0} = \begin{cases} \dfrac{1+\mu}{\Delta_0}\left(\dfrac{\Delta}{\mathcal{E}_{\max}}\right)^{\mu}, & \text{for } 0 \leqslant \Delta \leqslant \mathcal{E}_{\max} \\ & \text{and } \mathcal{E}_{\min} \leqslant \Delta_0 \leqslant \mathcal{E}_{\max}; \\ 0, & \text{otherwise.} \end{cases} \tag{4}$$

In this equation, $\mu < 1$ is a small positive parameter and $\mathcal{E}_{\max}$ is a maximum energy cutoff dictated by the energy scales of the system under consideration (see Sec. III B).

The interaction energy between any pairs of TLSs is assumed to be a function of their spatial separation r,

$$U(r) = \frac{U_0}{r^3}, \tag{5}$$

where U_0 is a material-dependent parameter associated with electric or elastic interactions. It is worth noting that interactions can occur between pairs of Q-TLSs or T-TLSs as well as between a T-TLS and a Q-TLS.

In the study of superconducting planar qubits, both f_{q} and T_1 are affected by the interactions hypothesized in the GTM. These types of qubits interact (semi)resonantly with an ensemble of Q-TLSs, where each Q-TLS can strongly interact with one or more T-TLSs. Such interactions lead to stochastic fluctuations in T_1 and f_{q}.

B. Qubit–Q-TLS interaction

The interaction between a qubit and a single Q-TLS leads to perturbations in T_1 and f_{q}. These perturbations depend on the coupling strength between the qubit and Q-TLS, g, and on the difference between the Q-TLS transition frequency $f_{\text{Q-TLS}}$ and f_{q}, $\Delta f = f_{\mathrm{q}} - f_{\text{Q-TLS}}$. In this work, we consider only T_1

fluctuations because, for a tunable qubit, f_{q} fluctuations are dominated by other noise processes such as flux noise.

In the rotating frame of the qubit and after a rotating-wave approximation, the Hamiltonian of the qubit coupled to the Q-TLS reads as

$$\widehat{H}_{\mathrm{q,Q\text{-}TLS}} = h\Delta f\, \hat{\sigma}_{\mathrm{q}}^{+}\hat{\sigma}_{\mathrm{q}}^{-} + hg(\hat{\sigma}_{\mathrm{q}}^{+} \otimes \hat{\sigma}_{\mathrm{Q\text{-}TLS}}^{-} + \mathrm{H.c.}), \quad (6)$$

where $\hat{\sigma}_{\mathrm{q}}^{\mp}$ and $\hat{\sigma}_{\mathrm{Q\text{-}TLS}}^{\mp}$ are the qubit and Q-TLS lowering and raising operators in the energy basis and H.c. is the Hermitian conjugate of the first term in parentheses. The coupling strength g is due to the electric dipole moment $\vec{p}$ of the Q-TLS and the electric field $\vec{E}_{\mathrm{q}}$ of the qubit,[2] $hg = \vec{p}\cdot\vec{E}_{\mathrm{q}}$.

The contribution to the energy relaxation rate of the qubit due to the Q-TLS can be approximated by

$$\Gamma_1^{\mathrm{q,Q\text{-}TLS}} = \frac{\Gamma_1^{\mathrm{Q\text{-}TLS}} - \widetilde{\Gamma}_1^{\mathrm{q}} - \mathrm{Re}[\Lambda]}{2}, \quad (7)$$

where $\Gamma_1^{\mathrm{Q\text{-}TLS}}$ is the energy relaxation rate of the Q-TLS due to phononic interactions with the environment, $\widetilde{\Gamma}_1^{\mathrm{q}}$ is the bare energy relaxation rate of the qubit,[3] and

$$\Lambda = \sqrt{\left(\widetilde{\Gamma}_1^{\mathrm{q}} + 2i(2\pi\Delta f) - \Gamma_1^{\mathrm{Q\text{-}TLS}}\right)^2 - 16(2\pi g)^2}, \quad (8)$$

with $i^2 = -1$. Equation (7) is valid when $\Gamma_1^{\mathrm{Q\text{-}TLS}} > \widetilde{\Gamma}_1^{\mathrm{q}}$, which is typically the case in our devices. The derivation of Eq. (7) is shown in Appendix A.

In presence of amorphous dielectric materials, the qubit is coupled to an ensemble of Q-TLSs. In this case, Eq. (7) represents the individual contribution to the energy relaxation rate of the qubit due to the kth Q-TLS, $\Gamma_1^{\mathrm{q,Q\text{-}TLS}} \to \Gamma_1^{\mathrm{q},k}$; each Q-TLS is now characterized by its own coupling strength g_k, frequency f_k, and energy relaxation rate Γ_1^k. The effective qubit relaxation rate is therefore given by

$$\Gamma_1^{\mathrm{q}} = \frac{1}{T_1} = \widetilde{\Gamma}_1^{\mathrm{q}} + \sum_k \Gamma_1^{\mathrm{q},k}. \quad (9)$$

C. Q-TLS–T-TLS interaction

We intend to calculate the frequency shift experienced by a Q-TLS due to the interaction with a T-TLS. We assume that the unperturbed energy and eigenstates are $E = E_{\mathrm{T\text{-}TLS}}$ and $\{|-\rangle, |+\rangle\}$ for the T-TLS and $E = E_{\mathrm{Q\text{-}TLS}} \gg E_{\mathrm{T\text{-}TLS}}$ and $\{|0\rangle, |1\rangle\}$ for the Q-TLS. These two TLSs form a quantum-mechanical system with Hamiltonian given by Eq. (11) in the work of Ref. [23]. Assuming the interaction energy U between the T-TLS and Q-TLS is given by Eq. (5), the four eigenenergies of the system are

$$E_0^{\mp} = -\frac{E_{\mathrm{Q\text{-}TLS}}}{2} \mp \sqrt{\left(\frac{E_{\mathrm{T\text{-}TLS}}}{2}\right)^2 + U\Delta + U^2} \quad (10a)$$

and

$$E_1^{\mp} = +\frac{E_{\mathrm{Q\text{-}TLS}}}{2} \mp \sqrt{\left(\frac{E_{\mathrm{T\text{-}TLS}}}{2}\right)^2 - U\Delta + U^2}, \quad (10b)$$

where Δ is the asymmetry energy of the T-TLS.

The frequency shift $\delta f^{\mp}$ of the Q-TLS due to the interaction with the T-TLS reads as

$$h\,\delta f^{\mp} = E_1^{\mp} - E_0^{\mp} - E_{\mathrm{Q\text{-}TLS}}, \quad (11)$$

which is negative when the T-TLS is in $|-\rangle$ and positive otherwise.

A T-TLS is thermally activated because of the condition $E_{\mathrm{T\text{-}TLS}} < k_{\mathrm{B}}T$ and, thus, switches state in time. This causes the sign of $\delta f^{\mp}$ to change, affecting the time evolution of the frequency of the Q-TLS coupled to it.

D. Qubit stochastic fluctuations

We assume that the state of a T-TLS over time is modeled by an RTS with switching rate

$$\gamma = \gamma_0 \exp\left(-\frac{V}{k_{\mathrm{B}}T}\right), \quad (12)$$

where γ_0 is a heuristic proportionality constant and V is implicitly given by Eq. (1).

A Q-TLS is generally coupled to several T-TLSs, where the ℓth T-TLS is characterized by a certain value of γ_ℓ and $\delta f_\ell^{\mp}$. Given the state ($|\mp\rangle$) of each T-TLS at a time t, we can approximate the effective frequency shift of the Q-TLS by summing the individual values of $\delta f_\ell^{\mp}(t)$. Since the T-TLS state is modeled by an RTS, the effective shift varies with t leading to a time series

$$f_{\mathrm{Q\text{-}TLS}}(t) = \frac{E_{\mathrm{Q\text{-}TLS}}}{h} + \sum_\ell \delta f_\ell^{\mp}(t). \quad (13)$$

For the kth Q-TLS, f_k fluctuates in time according to Eq. (13). As a consequence, Γ_1^{q} fluctuates because of its dependence on $\Gamma_1^{\mathrm{q},k}$, which, in turn, depends on f_k through Eq. (8). The stochastic fluctuations of $\Gamma_1^{\mathrm{q}} = 1/T_1$ are the main subject of this paper.

III. METHODS

In this section, we describe the methods used to perform the experiments on T_1 fluctuations (Sec. III A) and the corresponding simulations (Sec. III B).

A. Experiments

In this work, we use an Xmon transmon qubit to probe TLS defects. The main goal of our experiments is to characterize fluctuations in T_1 over long time periods and for different values of f_{q}. We measure T_1 by means of a standard energy relaxation experiment, a "T_1 experiment." Details on the qubit and setup are given in Appendix B.

In a T_1 experiment, we prepare the qubit in the excited state $|\mathrm{e}\rangle$ by means of a π pulse. We then measure the average population of $|\mathrm{e}\rangle$, P_{e}, for many values of a delay time spaced logarithmically between 1 ns and 200 μs. Due to the various relaxation channels affecting the qubit, including TLS interactions, P_{e} decays exponentially in time. We obtain T_1 by fitting the exponential decay and acquire between 36 and 38 points for each T_1 experiment.

[2]The electric field $\vec{E}_{\mathrm{q}}$ is the field associated with the qubit capacitor, which is described in Sec. III A and Appendix E.

[3]This is the rate caused by all dissipation sources other than TLSs.

TABLE I. Experimental parameters for the three data sets introduced in Sec. IV.

Data set	N_f (−)	f_q range (GHz)	Δt (s)	t_obs (h)
1	16	[4.369,4.669]	640	42.5
2	31	[4.500,4.560]	1000	47.2
3	31	[4.500,4.530]	1000	48.1

We measure T_1 for different values of f_q by setting a quasistatic flux bias ϕ_Z^qs applied to the qubit. The correspondence between ϕ_Z^qs and f_q is obtained from a qubit parameter calibration. Depending on the experiment, we set f_q over different bandwidths varying between 30 and 300 MHz. We select N_f linearly spaced values of f_q for each T_1 experiment. The T_1 measurements are repeated continuously at a repetition period Δt over an observation time t_obs, leading to matrices of data points as detailed in Appendix C. These matrices constitute the spectrotemporal charts of T_1 presented in Sec. IV. The experimental parameters for the three data sets shown in this work are reported in Table I.

B. Simulations

The procedure to simulate the effect of TLSs on the stochastic fluctuations in T_1 is composed of three main steps: (I) Generate an ensemble of Q-TLSs interacting with the qubit. (II) Generate several T-TLSs interacting with each Q-TLS. (III) Generate a time series for each T-TLS and propagate the effect of the T-TLSs' switching state to each Q-TLS, and, finally, to the qubit.

Before detailing each step of the procedure, it is worth introducing a few general assumptions:

(i) We consider that all TLSs are distributed uniformly in the oxide layers at the SA and MA interfaces of the qubit device. The thickness of these layers is assumed to be $t_\mathrm{ox} = 3\,\mathrm{nm}$ for both interfaces [18,33,34].

(ii) All the TLS parameters used in this procedure are assumed to be fixed for the entire duration of each simulation (see Appendix D); for each T-TLS, for example, γ is constant in time.

(iii) We assume that all T-TLSs belong to a single species (see Sec. V A).

(iv) We set $\widetilde{\Gamma}_1^\mathrm{q} = 1/27\,\mathrm{MHz}$, which is the value estimated for our device.

(v) For all distributions used in this work, we determine the probability density function (PDF) by normalizing a given distribution [e.g., that represented by Eq. (4)] over the chosen boundary values; we also find the cumulative density function (CDF). In order to pick a random value from a distribution, we generate a random quartile value between 0 and 1. We then calculate the random value corresponding to the generated quartile either by inverting the CDF or via root finding.

For step (I), we follow a similar procedure as in the work of Ref. [7]. Each Q-TLS is characterized by a 3-tuple of fundamental parameters $(f_\text{Q-TLS}, g, \Gamma_1^\text{Q-TLS})$. We pick $f_\text{Q-TLS}$ uniformly at random from a frequency range relevant to our experiments. Since $f_\mathrm{q} \sim 4.5\,\mathrm{GHz}$, we generate Q-TLSs with $f_\text{Q-TLS} \in [4, 5]\,\mathrm{GHz}$.

In order to generate g, we need a numerical value for both the effective electric dipole moment, $\tilde{p}$,[4] and $||\vec{E}_\mathrm{q}||$ at the position of the Q-TLS.

We pick $\tilde{p}$ from a known probability density that has been experimentally measured, e.g., in the work of Ref. [8],

$$f_{\tilde{p}} = \begin{cases} \dfrac{1}{\tilde{p}}\sqrt{1-\left(\dfrac{\tilde{p}}{\tilde{p}_\mathrm{max}}\right)^2}, & \text{for } \tilde{p}_\mathrm{min} \leqslant \tilde{p} \leqslant \tilde{p}_\mathrm{max}; \\ 0, & \text{otherwise.} \end{cases} \quad (14)$$

In this equation, we set the minimum and maximum value of $\tilde{p}$ to be $\tilde{p}_\mathrm{min} = 0.1\,\mathrm{debye}$ and $\tilde{p}_\mathrm{max} = 6\,\mathrm{debye}$; we choose $\tilde{p}_\mathrm{max}$ as in Ref. [7] and $\tilde{p}_\mathrm{min}$ assuming that any smaller dipole moment is negligible.

The position of a Q-TLS can be randomly picked at any point within the qubit oxide layers. We may then determine $\vec{E}_\mathrm{q}$ at each of these points by means of a conformal mapping technique. This technique allows us to transform the electric field of the qubit capacitor, $\vec{E}_\mathrm{q}$, into the known field of a parallel-plate capacitor. Details on this procedure are given in Appendix E.

Finally, we assume that $\Gamma_1^\text{Q-TLS} \propto \Delta_0^2$ [3], where the tunneling energy of the Q-TLS, Δ_0, is picked from an inverse probability distribution. We choose the bounds such that the resulting decay rates range between 1 and 100 MHz, with most rates at the low end of this range.

In order to complete step (I), we need to know the total number of Q-TLSs, $N_\text{Q-TLS}$, and their associated 3-tuple parameters. The Q-TLSs are hosted within an interaction region with volume determined by the length of the two CPW segments forming the qubit Al island (see Appendix B) and the same cross-sectional area used to pick $\vec{E}_\mathrm{q}$ (see Appendix E), $V_\mathrm{int} = 96\,\mu\mathrm{m} \times 3\,\mathrm{nm} \times 376\,\mu\mathrm{m} \times 2$. Given a Q-TLS bandwidth $B_\text{Q-TLS} = 1\,\mathrm{GHz}$, assuming a Q-TLS density $D = 200\,\mathrm{GHz}^{-1}\,\mu\mathrm{m}^{-3}$ (see Sec. V B), and disregarding all Q-TLSs with $g < 70\,\mathrm{kHz}$, we obtain $N_\text{Q-TLS} \sim 570$.

In step (II), each T-TLS is characterized by a 2-tuple of fundamental parameters $(\delta f^{\mp}, \gamma)$. We generate $\delta f^{\mp}$ from Eq. (11), where Δ and Δ_0 are picked from the GTM distribution of Eq. (4). We assume $\mathcal{E}_\mathrm{min}/h = 125\,\mathrm{MHz}$, $\mathcal{E}_\mathrm{max}/h = 1\,\mathrm{GHz}$, and $\mu = 0.3$ [23]. The interaction energy $U(r)$ is calculated from Eq. (5), where $U_0 = k_\mathrm{B} \times 10\,\mathrm{K\,nm}^3$ and r is the Q-TLS–T-TLS distance; this distance must be picked at random. Given a cylindrical region with radius r and height t_ox centered on the Q-TLS and a uniform T-TLS density, the CDF for the number of T-TLSs is proportional to r^2. As a consequence, the PDF is linear in r, $f_r \propto r$. We pick r from f_r assuming $r_\mathrm{min} = 15\,\mathrm{nm}$ and $r_\mathrm{max} = 60\,\mathrm{nm}$ as bounds (see Sec. V B for a discussion on r_max).

We then generate γ from Eq. (12). In addition to the parameters used to generate $\delta f^{\mp}$, we need $T = 60\,\mathrm{mK}$, $\gamma_0 \approx 0.4\,\mathrm{Hz}$, $\Omega_0 = 1\,\mathrm{GHz}$, $m = 16\,\mathrm{u}$, and $d = 2\,\mathrm{Å}$ (see Sec. V A for a discussion on the physical meaning of these parameters). Note that the effective qubit temperature $T = 60\,\mathrm{mK}$ corresponds

[4]The angle η between $\vec{p}$ and $\vec{E}_\mathrm{q}$ is integrated in the distribution for $\tilde{p}$, i.e., $\tilde{p} = ||\vec{p}|| \cos\eta$ [8].

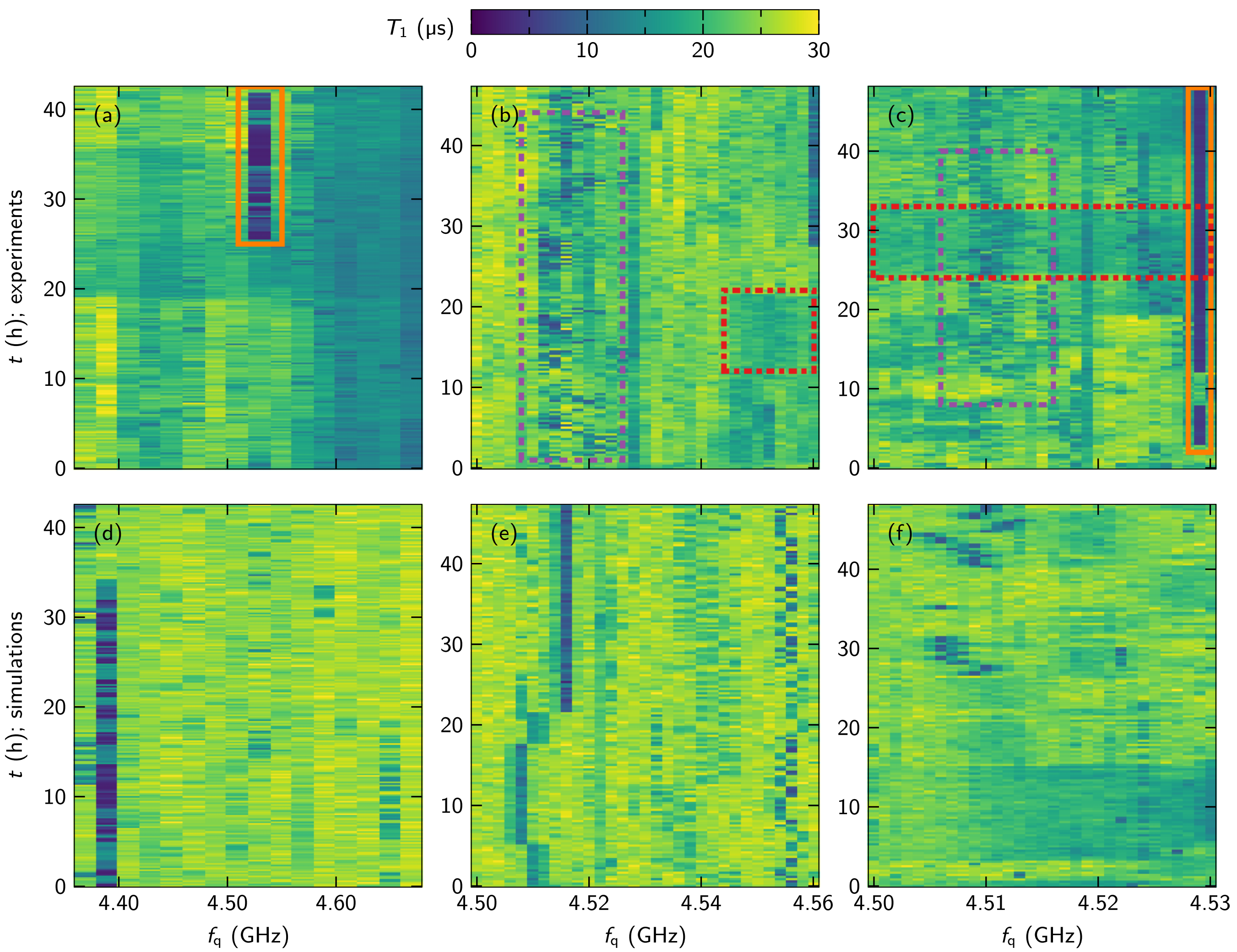

FIG. 1. Experimental [(a), (b), and (c); data sets 1, 2 and 3, respectively, in Table I] and simulated [(d), (e), and (f)] spectrotemporal charts of T_1 vs f_q and t, where the panels in each column display an experiment and the corresponding simulation. Spectral-diffusion patterns in the experiments are highlighted with boxes. Band-limited diffusive: dashed purple boxes. Fast narrow-band telegraphic: solid orange boxes. Slow wide-band telegraphic: dashed-dotted red boxes. In the simulations, we add a background time series of Gaussian white noise with a standard deviation of 2 kHz, which is comparable to the fitting error of our T_1 experiments.

to a qubit ground-state population of 2.7 %, which is approximately the value observed in our experiments.

Similarly to step (I), in order to complete step (II) we need to select the number of T-TLSs interacting with each Q-TLS, $N_{\text{T-TLS}}$. We generate a set of $N_{\text{T-TLS}} = 10$ T-TLSs, ensuring that each of them additionally fulfills the condition $E_0^+ - E_0^- = \sqrt{E_{\text{T-TLS}}^2 + 4U(\Delta + U)} < E_{\max} = k_B T/2$. We choose half of the thermal energy as our activation threshold, although similar values would work as well.

In step (III), we generate the simulated spectrotemporal charts for Γ_1^q (and, thus, T_1). Stochastic fluctuations are due to a T-TLS switching state randomly between the left and right well. We simulate these fluctuations as an RTS with a single γ for both the left and right well, i.e., assuming a symmetric noise process. For an RTS, the probability of spending a time t in a certain state is given by the PDF $f_t = \gamma\ \exp(-\gamma t)$. Starting from a random state, we produce a list of times spent in each T-TLS state until reaching t_{obs}. In order to generate a time series for the T-TLS state, we sample the time list at Δt intervals. The values of both Δt and t_{obs} used in the simulations are the same as for the experiments and are reported in Table I.

The T-TLS state corresponds to a particular $\delta f^{\mp}$. Therefore, as explained in Sec. II D, the time series $f_{\text{Q-TLS}}(t)$ for each Q-TLS can be calculated by means of Eq. (13). Finally, we evaluate Eq. (9) for all values of interest of f_q; in order to match the spectrotemporal charts measured in the experiment, we choose f_q and N_f for the ranges and values reported in Table I.

The simulations are performed using the Julia Programming Language [35]. The computer code QUBITFLUCTUATIONS.JL can be obtained from a GitLab repository [36].

IV. RESULTS

The main results of this work are presented in Fig. 1, which shows the experimental and simulated spectrotemporal charts

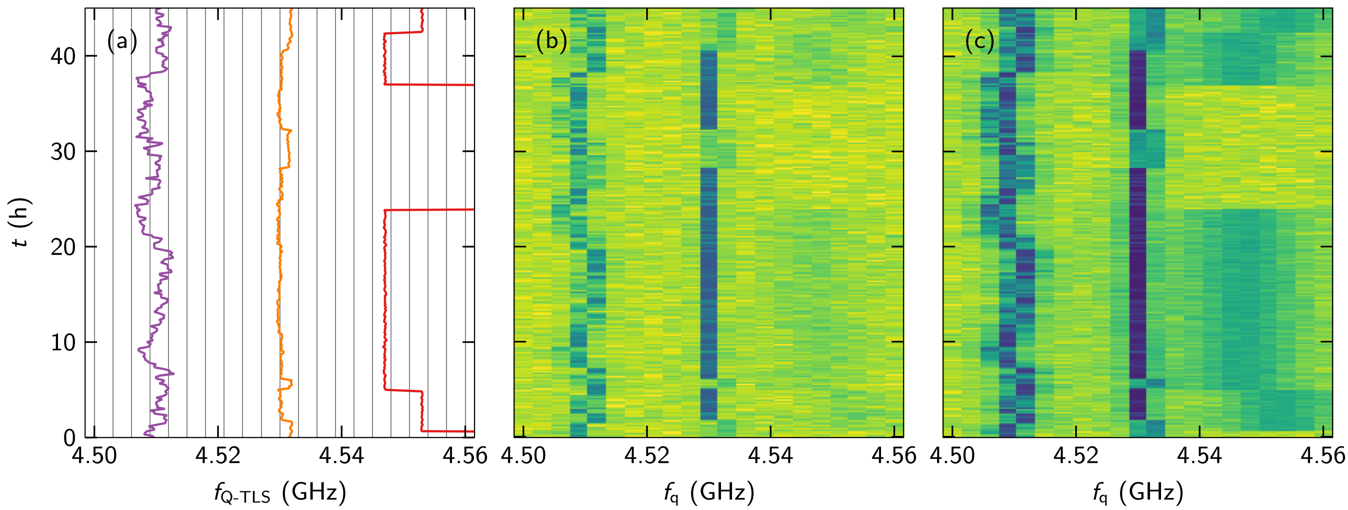

FIG. 2. Three spectral-diffusion patterns. (a) Q-TLS frequency $f_{\text{Q-TLS}}$ vs t for Q-TLS 1 (left purple line), 2 (middle orange line), and 3 (right red line). (b), (c) Simulated spectrotemporal charts of T_1 vs f_q and t for $g = 50$ and 100 kHz, respectively. The color map for T_1 is the same as in Fig. 1.

of T_1. Details on the experiments and simulations are described in Secs. III A and III B, respectively, with parameters reported in Table I. Each realization of a simulation is random due to the very nature of the method (because, e.g., $f_{\text{Q-TLS}}$ is distributed uniformly). We thus choose to display simulated spectrotemporal charts that resemble the experiments.

A visual inspection of the T_1 stochastic fluctuations in Fig. 1 reveals three distinct spectral-diffusion patterns:

(1) Band-limited diffusive.

(2) Fast narrow-band telegraphic.

(3) Slow wide-band telegraphic.

Generally, it is also possible to observe combinations of such patterns.

The three patterns can be qualitatively explained by performing *ad hoc* simulations using a similar method as in Sec. III B. However, instead of randomly generating the 3- and 2-tuple of steps (I) and (II), we set these tuples by hand. We simulate the effect of several T-TLSs on one Q-TLS, considering three T-TLS sets with different ranges of $\delta f^{\mp}$ and γ. For clarity, we choose three Q-TLSs with distinct values of $f_{\text{Q-TLS}}$, Q-TLS 1, 2, and 3, one for each set of T-TLSs.

In broad strokes, the band-limited diffusive process is reproduced by simulating the effect of many ($\sim$10) T-TLSs on Q-TLS 1; we select T-TLSs with low values of $1/\gamma$ (ranging between tens of minutes and hours) and small values of $\delta f^{\mp}$ (<1 MHz). The fast narrow-band telegraphic process, instead, is generated by considering a few ($\lesssim$3) T-TLSs acting on Q-TLS 2; in this case, we select high values of $1/\gamma$ (on the order of hours) as well as small values of $\delta f^{\mp}$ (<1 MHz). Similarly to the case of the fast narrow-band process, the slow wide-band telegraphic process is created assuming also a few ($\lesssim$3) T-TLSs, this time coupled to Q-TLS 3; in this instance, however, we select very high values of $1/\gamma$ (on the order of days) and large values of $\delta f^{\mp}$ ($\leqslant$ 20 MHz). Figure 2 illustrates the results of the simulation of the three patterns. Figure 2(a) exemplifies the effect of the three different sets of T-TLSs on Q-TLS 1, 2, and 3. Figures 2(b) and 2(c) demonstrate the impact of each Q-TLS on the spectrotemporal chart of T_1 for a small (a) and large (b) value of g. The T-TLS and Q-TLS parameters used in the simulations are reported in Table II.

Q-TLS 1 is affected by many T-TLSs that switch continuously during observation. The T-TLSs act additively on the Q-TLS, resulting in a diffusive shift of $f_{\text{Q-TLS}}$ [see Eq. (13)]. Different from Brownian diffusion, the shift in $f_{\text{Q-TLS}}$ does not exceed the sum of the individual frequency shifts induced by each T-TLS at any observation time. The diffusive process is thus characterized by a limited frequency bandwidth, as shown in Fig. 2(a). The spectrotemporal chart of T_1 displays a similar behavior; T_1 fluctuates in time over a finite-frequency range, exhibiting moderate and strong variations in Figs. 2(b) and 2(c), respectively.

Q-TLS 2, which is affected by a few T-TLSs, switches mainly between two values of $f_{\text{Q-TLS}}$ (low and high); for both states, much smaller fluctuations at higher switching rates are noticeable. The telegraphic nature of this process affects

TABLE II. T-TLS and Q-TLS parameters used in the simulations of Fig. 2.

Q-TLS	$f_{\text{Q-TLS}}$ (GHz)	$\Gamma_1^{\text{Q-TLS}}$ (MHz)	γ (Hz)	$\delta f^{\mp}$ (MHz)
1	4.510	10	2×10^{-5}	0.9
			5×10^{-5}	0.7
			8×10^{-5}	0.7
			1×10^{-4}	0.6
			2×10^{-4}	0.6
			3×10^{-4}	0.5
			4×10^{-4}	0.3
			1×10^{-3}	0.1
2	4.531	5	3×10^{-5}	0.8
			8×10^{-5}	0.2
			2×10^{-4}	0.1
3	4.570	90	6×10^{-6}	20
			8×10^{-6}	3

dramatically the spectrotemporal chart of T_1 when $f_{\text{Q-TLS}} \simeq f_q$. This is the case in the example of Fig. 2(a) when Q-TLS 2 dwells in the low-frequency position. In this state, T_1 becomes largely reduced compared to when the Q-TLS resides in the high-frequency position, as displayed in Figs. 2(b) and 2(c). The low value of $\Gamma_1^{\text{Q-TLS}}$ leads to a narrow-band process, with more pronounced T_1 variations in Fig. 2(b) compared to Fig. 2(c).

It is worth noting that, in our example, the high-frequency position lies between two values of f_q [vertical solid light-gray lines in Fig. 2(a)] but is too far from either of them to significantly impact T_1. This effect shows that the frequency resolution of our experiments [i.e., the x-axis "pixeling" in Figs. 2(b) and 2(c) and, thus, in Fig. 1] affects the spectrotemporal chart of T_1.

Q-TLS 3 behaves similarly to Q-TLS 2, although one of the T-TLSs has a significantly larger value of $\delta f^{\mp}$. Due to low values of γ, Q-TLS 3 undergoes telegraphic frequency shifts only a couple of times during observation. The high value of $\Gamma_1^{\text{Q-TLS}}$ strongly damps the effect on T_1, resulting in a wide-band process. In fact, the effect is barely visible in Fig. 2(b), even when the Q-TLS is almost on resonance with the qubit. In presence of a strong coupling, however, the impact on the spectrotemporal chart of T_1 is clearly identifiable; as shown in Fig. 2(c), the effect extends over a large frequency range.

V. DISCUSSION

In this section, we discuss the physical characteristics of a T-TLS (Sec. V A); we then discuss the density of TLSs (Sec. V B); finally, we provide insight on the interpretation of the Allan deviation and power spectral density (Sec. V C).

A. Physical characteristics of a T-TLS

The two quantities required to represent T-TLSs in the simulations shown in Fig. 1 are $\delta f^{\mp}$ and γ of Eqs. (11) and (12), respectively. The former is determined only by parameters chosen according to the GTM. The latter requires the knowledge of additional physical characteristics of T-TLSs: m and d, as well as Ω_0; explicitly,

$$\gamma = \gamma_0 \exp\left[-\left(\frac{\hbar}{d}\right)^2 \frac{1}{2m}\left(\ln\frac{h\Omega_0}{\Delta_0}\right)^2 \Big/ (k_B T)\right]. \tag{15}$$

The T-TLS mass m must be between that of a very light element such as an electron and that of heavier elements such as atoms or molecules. That is, it can vary over several orders of magnitude. The interwell distance d should be on the order of angstroms. Electrons and atoms cannot get displaced by more than the interatomic bond length. In the case of molecules, the commonly accepted fluctuation model involves the collective motion of atoms, where each individual atom also cannot move more than the interatomic bond length [2,31].

In our simulations, we assume a single species of T-TLSs. In order to obtain simulated spectrotemporal charts that resemble the experimental ones, the product d^2m in Eq. (15) must lie within one order of magnitude of 10^{-45} m^2 kg. Considering that d is confined within a few angstroms, the value of m cannot be chosen arbitrarily. If there was clear evidence of multiple T-TLS species characterized by different ranges of γ, they could be modeled assuming different values of m and d. For example, lighter particles would have higher values of γ.

We assume that TLSs, and thus T-TLSs, are hosted in *oxide* layers at the SA and MA interfaces (see Sec. III B; we assume the SM interface to be clean due to our fabrication process). The oxide layers are composed of molecules with an oxygen (O) atom bound to a pair of neighboring atoms. A T-TLS can be modeled as an *O atom* with mass $m = 16$ u tunneling between two wells (i.e., states) at a distance d from each other. It is reasonable to assume that d is comparable to the bond length between the O atom and a neighboring atom [3]. In many applications, using Si or sapphire substrates and Al as a metal results in amorphous Si or Al oxide interfacial layers. The bond length between the O and Si or Al atoms is on the order of 2 Å [37,38]; this is why in our simulations we choose $d = 2$ Å.

Equation (1) is valid only when $V \geqslant 0$. Accordingly, it must be that $h\Omega_0 \geqslant \Delta_0$ for all values of Δ_0 picked from the GTM distribution. On the one hand, choosing a value $h\Omega_0 \sim \Delta_0$ leads to $V \sim 0$, which would correspond to a single- rather than a double-well potential. On the other hand, we cannot choose Ω_0 to be arbitrarily large due to its relationship to γ in Eq. (15). In fact, there is a small range of values of Ω_0 that result in a distribution of γ similar to that empirically inferred from the spectrotemporal charts of Fig. 1. We choose $\Omega_0 = 1$ GHz to match the experimental range $\gamma \in [10^{-6}, 10^{-2}]$ Hz (i.e., a period from days to minutes) as closely as possible. In this case, we obtain T-TLSs with $V/h \gtrsim 1.8$ GHz.

B. Density of TLSs

The TLS density D is estimated by counting the number N of TLSs within a certain interaction region with volume V_{int} and bandwidth B, $D = N/(V_{\text{int}} B)$. In the case of Q-TLSs, their number $N_{\text{Q-TLS}}$ can be readily obtained by counting the interactions between a qubit and a Q-TLS in spectroscopy experiments [5,7,17,39]. For qubits where Q-TLSs are hosted in a volume of native oxide, the estimated density is $D_{\text{Q-TLS}} \sim 100\ \text{GHz}^{-1}\ \mu\text{m}^{-3}$. In order to reproduce well our experimental spectrotemporal charts, in the simulations we choose $D_{\text{Q-TLS}} = 200\ \text{GHz}^{-1}\ \mu\text{m}^{-3}$.

Spectroscopic methods cannot be used to count the number of T-TLSs because, at such low frequencies, the qubit is in an incoherent thermal state. The experimental spectrotemporal charts reveal that Q-TLSs are generally affected by multiple sources of telegraphic noise, as clearly shown by the band-limited diffusive pattern in Fig. 1. This observation makes it possible to infer the number of T-TLSs coupled to each Q-TLS, $N_{\text{T-TLS}}$; in the simulations, we choose $N_{\text{T-TLS}} = 10$. These T-TLSs are assumed to be contained inside an interaction region with volume V_{int} centered on their host Q-TLS. It is worth pointing out that our choice of $N_{\text{T-TLS}} = 10$ can still result in both the fast narrow-band and slow wide-band telegraphic patterns in Fig. 1; this is because $\delta f^{\mp}$ and γ are distributed over a large parameter range possibly leading to a single predominant T-TLS.

The experiment of Fig. 1(c) allows us to resolve T-TLSs with interaction strengths $U(r)/h \geqslant 1$ MHz. According to Eq. (5), this condition corresponds to a maximum interaction distance $r_{max} = 60$ nm. Notably, this condition is similar to that hypothesized in the work of Ref. [23]. As explained in Sec. III B, the T-TLS interaction region is a cylinder with radius r_{max} and a height of t_{ox}; the volume associated with this region is $V_{int} \approx 3.4 \times 10^{-5}$ μm^{-3}.[5]

Given $B = (E_{max} - E_{min})/h = 500$ MHz, we finally obtain $D_{T\text{-}TLS} \approx 6 \times 10^5$ GHz^{-1} μm^{-3}. This value is much larger than $D_{Q\text{-}TLS}$, suggesting that D varies significantly in frequency and is higher at lower frequencies. This finding is in contrast with the typical assumption made by the STM practitioners that TLSs are uniformly distributed in frequency. It is worth noting that a result similar to ours has been recently reported in the work of Ref. [30], although our value for $D_{T\text{-}TLS}$ is even larger than in that work.

C. On the interpretation of the Allan deviation and power spectral density

Time series experiments similar to those reported here are frequently studied by means of statistical analyses such as the Allan deviation (AD) or the power spectral density (PSD), or both. For example, this approach has been pursued in the works of Refs. [27,28]. It is tempting to ascribe simple models to these statistical estimators in order to extract T-TLS parameters such as their switching rate γ and number $M_{T\text{-}TLS}$; in this case, $M_{T\text{-}TLS}$ is the total number of T-TLSs affecting the qubit by interacting with a single or multiple Q-TLSs. It is common, however, to encounter scenarios where these models are misleading.

Figure 3 presents two distinct scenarios that illustrate this issue. The time series in Fig. 3(a) are obtained by simulating one scenario with $M_{T\text{-}TLS} = 1$ and another with $M_{T\text{-}TLS} = 4$. The simulations parameters are reported in Table III. As expected, there is a stark visual difference between the two time series: In the first scenario, it is possible to clearly identify one RTS; this is impossible in the second scenario. However, this difference is not reflected in either the overlapping AD or PSD. In both simulated scenarios, we observe a pronounced peak in the overlapping AD and a lobe in the PSD. These features are indicative of Lorentzian noise. However, they appear to be practically the same for the two scenarios. In fact, it is possible to fit the overlapping AD or PSD using a simple model based on a single source of Lorentzian noise, along with white noise. The model reads as

$$\sigma^2 = \frac{h_0}{2\tau} + \left(\frac{A_0\tau_0}{\tau}\right)^2\left(4e^{-\tau/\tau_0} - e^{-2\tau/\tau_0} - 3 + \frac{2\tau}{\tau_0}\right) \quad (16)$$

for the AD and

$$S = h_0 + \frac{4A_0^2\tau_0}{1 + (2\pi f\tau_0)^2} \quad (17)$$

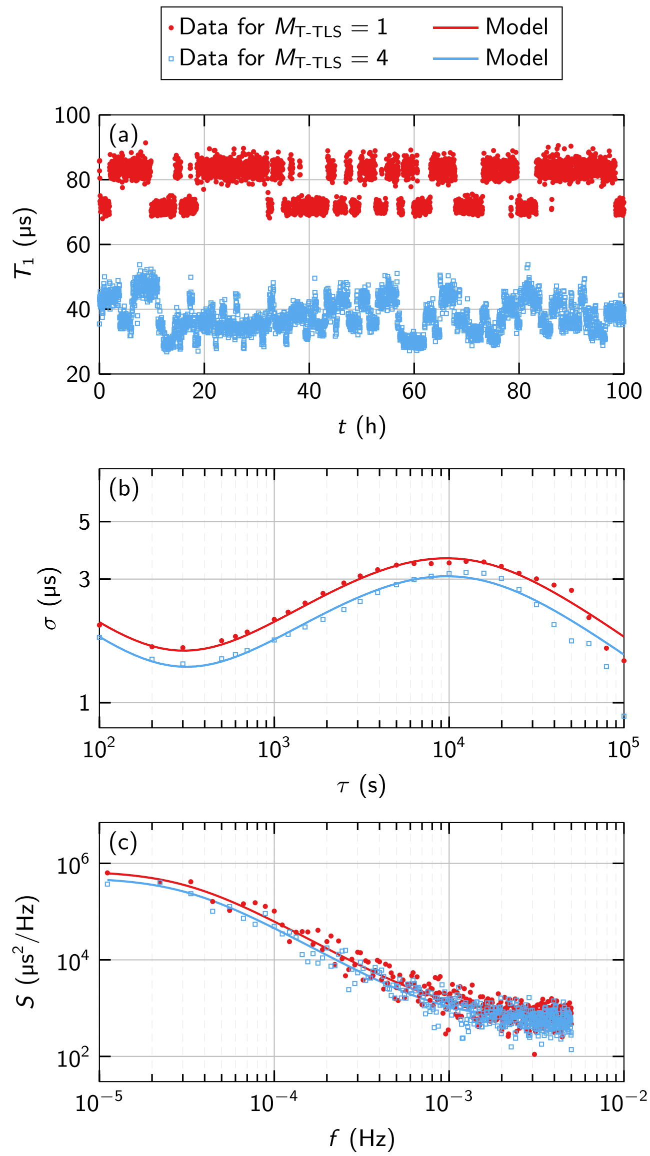

FIG. 3. Comparison between the statistical analyses of two simulated time series. (a) Simulated time series of T_1 vs t. The series for $M_{T\text{-}TLS} = 1$ is vertically offset by 40 μs for clarity. (b) Estimated overlapping AD σ vs τ and associated fitting curves from Eq. (16). We find $A_0 = 5.84(5)$ and $4.98(6)$ μs, $h_0 = 749(111)$ and $583(119)$ μs^2 Hz^{-1}, and $1/\tau_0 = 195(7)$ and $195(10)$ μHz for $M_{T\text{-}TLS} = 1$ and 4, respectively. Note that we are fitting σ^2 with the Levenberg-Marquardt algorithm but plotting σ. The overlapping AD is computed at logarithmically spaced points. (c) Estimated PSD S vs f. We use the fitting parameters from (b) to overlay the model of Eq. (17) to the data. The PSD is estimated using the Welch's method with 25 h overlapping segments (rectangular window). The value of τ_0 fitted for $M_{T\text{-}TLS} = 1$ matches (within the confidence interval) that chosen in the simulations and reported in Table III; the fitted τ_0 for $M_{T\text{-}TLS} = 4$, instead, does not match any of the values in Table III.

for the PSD, where τ and f are the analysis interval and frequency, h_0 and A_0 are the white and Lorentzian noise amplitudes, and τ_0 is the Lorentzian characteristic time [40].

Although the two simulated time series are associated with entirely different scenarios, the simple models of Eqs. (16)

[5]For the Q-TLS density used in our simulations, $D_{Q\text{-}TLS} = 200$ GHz^{-1} μm^{-3}, we can find a Q-TLS area density $\sigma_{Q\text{-}TLS} = D_{Q\text{-}TLS} \times 1$ GHz $\times$ 3 nm $= 0.6$ μm^{-2}. The average area per Q-TLS is therefore $1/\sigma_{Q\text{-}TLS}$. Assuming each Q-TLS is contained within a square, the radius of the circle inscribed in each square is $r_{Q\text{-}TLS} = \sqrt{1/\sigma_{Q\text{-}TLS}}/2 \approx 600$ nm. Since $r_{max} \ll r_{Q\text{-}TLS}$, the T-TLS interaction regions do not overlap on average and, thus, we are not double counting T-TLSs.

TABLE III. Time-series simulation parameters used in Fig. 3. The simulations are performed as described in Sec. III B; however, instead of randomly picking all relevant parameters, we manually specify them. Note that $\gamma = 1/(2\tau_0)$.

$M_{\text{T-TLS}}$	$f_{\text{Q-TLS}}$ (GHz)	g (MHz)	$\Gamma_1^{\text{Q-TLS}}$ (MHz)	γ (μHz)	$\delta f^{\mp}$ (MHz)
1	4.5011	0.04	15	100	0.6
4	4.5011	0.02	10	75	0.8
	4.5015	0.02	10	70	0.6
	4.4989	0.02	10	140	0.8
	4.4986	0.02	10	75	0.4

and (17) fit accurately both the overlapping AD and PSD for very similar values of τ_0; we obtain $1/\tau_0 = 195(7)\ \mu$Hz when $M_{\text{T-TLS}} = 1$ and $1/\tau_0 = 195(10)\ \mu$Hz when $M_{\text{T-TLS}} = 4$. This conclusion can be qualitatively understood by noticing that multiple physical sources of Lorentzian noise combine to form a single wide-band peak in the overlapping AD (or lobe in the PSD). As a consequence, this feature can be mistakenly fitted with a model comprising a single Lorentzian term. For this reason, we elect *not to analyze* our experimental results by ascribing simple models to the AD (or PSD).

VI. CONCLUSIONS

We study the physics of TLSs by means of a frequency-tunable planar superconducting qubit. We show that simulations based on the TLS interacting model (or GTM) can explain the spectrotemporal charts of T_1 observed in the experiments over long time periods. We find that the density of T-TLSs is much larger than that of Q-TLSs, meaning TLSs are nonuniformly distributed over large frequency bandwidths. Our finding corroborates the results reported in the work of Ref. [30].

Our experiments demonstrate that the additional dimension provided by frequency tunability makes tunable qubits a better probe to study spectral diffusion compared to fixed-frequency devices. Hence, we suggest that future work on TLS stochastic fluctuations should explore even wider frequency bandwidths. A large bandwidth would increase the chances to encounter a scenario where a pair of Q-TLSs interacts with a single T-TLS, resulting in a synchronous fluctuation of the two Q-TLSs. Such an experiment would conclusively prove the validity of the TLS-TLS interaction hypothesis in the GTM.

It is well known that external strain or electric fields applied to a qubit chip modify the Q-TLSs' characteristic energies, Δ or Δ_0, or both [17]. Therefore, we suggest to apply external fields while exploring long-time qubit fluctuations. Such an experiment may make it possible to indirectly observe a similar change in the characteristic energies of the T-TLSs. In fact, both Δ and Δ_0 contribute to changes in $\delta f^{\mp}$, whereas γ is affected only by Δ_0. In principle, this procedure would allow us to perform an indirect spectroscopic study of T-TLSs as a function of external fields.

It is also worth noting that recent advances on the coupling of superconducting devices to bulk acoustic waves [41] may pave the way to the acoustic characterization of TLS-induced qubit loss and fluctuations.

Lastly, we expect that performing experiments at different operating temperatures would provide one more knob to modify the frequency bandwidth of thermally activated TLSs. This approach would allow us to characterize the TLS density for different frequency ranges.

ACKNOWLEDGMENTS

This research was undertaken thanks in part to funding from the Canada First Research Excellence Fund (CFREF). We acknowledge the support of the Natural Sciences and Engineering Research Council of Canada (NSERC), [Application Number: RGPIN-2019-04022]. We would like to acknowledge the Canadian Microelectronics Corporation (CMC) Microsystems for the provision of products and services that facilitated this research, including CAD software. The authors thank the Quantum-Nano Fabrication and Characterization Facility at the University of Waterloo, where the sample was fabricated. We acknowledge M. I. Dykman for his involvement in the early stages of this work.

APPENDIX A: DERIVATION OF $\Gamma_1^{\text{q,Q-TLS}}$

In this Appendix, we derive Eq. (7). The master equation in Lindblad form of a qubit–Q-TLS system reads as

$$\frac{d\hat{\rho}}{dt} = -\frac{i}{\hbar}[\widehat{H}_{\text{q,Q-TLS}}, \hat{\rho}] + \sum_j \left(\hat{L}_j\hat{\rho}\hat{L}_j^\dagger - \frac{1}{2}\{\hat{L}_j^\dagger\hat{L}_j, \hat{\rho}\}\right), \tag{A1}$$

where $\hat{\rho}(t)$ is the density matrix, $\widehat{H}_{\text{q,Q-TLS}}$ is given by Eq. (6), $j \in \{\text{q, Q-TLS}\}$, and $\hat{L}_j$ and $\hat{L}_j^\dagger$ are Lindblad operators.

Our study is focused on the fluctuations in T_1. Hence, in Eq. (A1) we only account for the energy relaxation rates of the qubit and Q-TLS. In this case, the Lindblad operators are $\hat{L}_{\text{q}} = \sqrt{\widetilde{\Gamma}_1^{\text{q}}}\,\hat{\sigma}_{\text{q}}^-$ and $\hat{L}_{\text{Q-TLS}} = \sqrt{\Gamma_1^{\text{Q-TLS}}}\,\hat{\sigma}_{\text{Q-TLS}}^-$.

The quantity $\hat{L}_j\hat{\rho}\hat{L}_j^\dagger = 0$ at all times because there is at most one excitation in a qubit–Q-TLS coupled system. With this assumption and by defining the effective non-Hermitian Hamiltonian [42]

$$\widehat{H}_{\text{eff}} = \widehat{H}_{\text{q,Q-TLS}} - \frac{i}{2}\left(\widetilde{\Gamma}_1^{\text{q}}\,\hat{\sigma}_{\text{q}}^+\hat{\sigma}_{\text{q}}^- + \Gamma_1^{\text{Q-TLS}}\,\hat{\sigma}_{\text{Q-TLS}}^+\hat{\sigma}_{\text{Q-TLS}}^-\right), \tag{A2}$$

the Lindbladian of Eq. (A1) can be written as a simple Schrödinger equation with a "decaying wave function" $|\Psi(t)\rangle = \alpha(t)|\text{e}\rangle + \beta(t)|1\rangle$, where $\alpha(t)$ and $\beta(t)$ are the time-dependent complex amplitudes associated with the excited state $|\text{e}\rangle$ of the qubit and $|1\rangle$ of the Q-TLS.

The exact result of the Schrödinger equation for $\alpha(t)$ given that $\alpha(t=0) = 1$ and $\beta(t=0) = 0$ is

$$\alpha(t) = \frac{1}{2\Lambda}\left[a\exp\left(-\frac{\Lambda}{4}t\right) + b\exp\left(\frac{\Lambda}{4}t\right)\right] \times \exp\left(-\frac{\widetilde{\Gamma}_1^{\text{q}} + \Gamma_1^{\text{Q-TLS}}}{4}t\right), \tag{A3}$$

where Λ is given by Eq. (8), $a = \Lambda - (\Gamma_1^{\text{Q-TLS}} - \widetilde{\Gamma}_1^{\text{q}}) + 4\pi i\Delta f$, and $b = \Lambda + (\Gamma_1^{\text{Q-TLS}} - \widetilde{\Gamma}_1^{\text{q}}) - 4\pi i\Delta f$.

Since we are calculating a decay, we are only interested in the envelope of $\alpha(t)$, $\tilde{\alpha}(t)$. We thus set $\mathrm{Im}[\Lambda] = 0$ in the two exponential terms of Eq. (A3) and calculate the envelope probability $\tilde{P}_e(t) = |\tilde{\alpha}(t)|^2$ for the qubit to be in $|e\rangle$:

$$\begin{aligned}\tilde{P}_e(t) = &\left|\frac{a}{2\Lambda}\right|^2 \exp\left[-\frac{\Gamma_1^{\text{Q-TLS}} + \widetilde{\Gamma}_1^{q} + \mathrm{Re}[\Lambda]}{2}t\right] \\ &+ \left|\frac{b}{2\Lambda}\right|^2 \exp\left[-\frac{\Gamma_1^{\text{Q-TLS}} + \widetilde{\Gamma}_1^{q} - \mathrm{Re}[\Lambda]}{2}t\right] \\ &+ \frac{ab^* + a^*b}{|2\Lambda|^2} \exp\left[-\frac{\Gamma_1^{\text{Q-TLS}} + \widetilde{\Gamma}_1^{q}}{2}t\right]. \qquad \text{(A4)}\end{aligned}$$

When $\Gamma_1^{\text{Q-TLS}} > \widetilde{\Gamma}_1^{q}$, which is the regime of interest in our experiments, the term proportional to $|b|^2$ in Eq. (A4) is dominant. Therefore, in order to find an approximate expression for the Q-TLS contribution only, we subtract the qubit contribution $\widetilde{\Gamma}_1^{q}$ from the rate in the exponential proportional to $|b|^2$. This procedure results in Eq. (7) in the main text.

APPENDIX B: DEVICE AND SETUP

The superconducting Xmon transmon qubit [7] used in this paper is the same as in our work of Ref. [5], with micrographs shown in that paper. The qubit consists of an Al island in parallel with a superconducting quantum interference device (SQUID).

The Al island forms a capacitor that is composed of two intersecting CPW segments in the shape of a Greek cross, where each segment has length $L = 376$ μm. One segment is formed by a center conductor, or strip, of width $S = 24$ μm and is separated by a distance $W = 24$ μm from a ground plane on each side of the strip. The capacitance of the island is $C_q \approx 100$ fF (corresponding to a single-electron charge energy $E_c/h \approx 188.6$ MHz).

The qubit capacitor is connected in parallel with the SQUID, which is made of an Al loop interrupted by two parallel Josephson tunnel junctions with critical current $I_{c0} \approx 17.4$ nA (corresponding to a Josephson energy $E_J/h \approx 8.6$ GHz) for each junction. The SQUID forms the inductive element of the qubit.

Due to the SQUID design, we are able to tune the SQUID critical current I_c *in situ* during the experiment by threading the SQUID loop with a flux $\phi_Z = M_Z\, i_Z$, where $M_Z \sim 3$ pH is the mutual inductance between the loop and an external circuit with current i_Z. A quasistatic flux bias ϕ_Z^{qs} allows us to set the qubit frequency $f_q(\phi_Z^{\text{qs}})$, i.e., the qubit bias point. The qubit parameters given above result in a zero-bias $f_q(\phi_Z^{\text{qs}} = 0) \approx 4.8$ GHz.

The qubit can be controlled by means of X or Y microwave pulses, which are applied through a capacitive network with coupling capacitor of capacitance $C_{XY} \approx 100$ aF. The qubit state is measured by means of a readout resonator with $f_r \approx 5$ GHz, which is capacitively coupled with a coupling capacitor of capacitance $C_M \approx 3.4$ fF. We read out the qubit state over 655 single-shot measurements to find P_e with a visibility $\gtrsim 90\,\%$.

The qubit is fabricated by depositing and patterning thin-film Al on thoroughly cleaned surfaces; we use the same cleaning process as in our work of Ref. [4]. The Josephson tunnel junctions are fabricated using a standard double-angle Niemeyer-Dolan technique. The qubit is operated at the base temperature of a dilution refrigerator, approximately 10 mK. The control and measurement signals are applied through a heavily filtered microwave network. The setup is the same as in our work of Ref. [5], which shows a detailed diagram of the control and measurement lines.

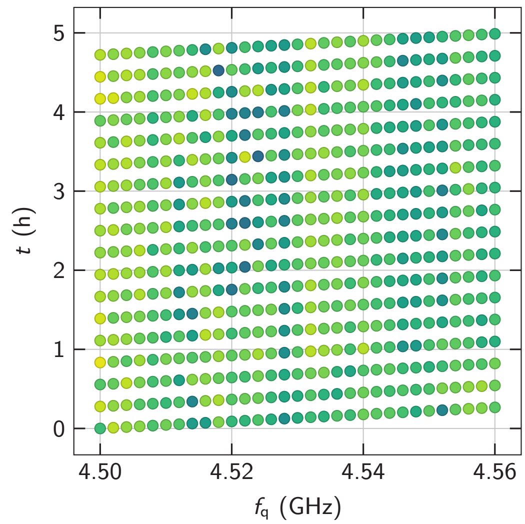

FIG. 4. Scatter plot of T_1 vs f_q and t for data set 2 [same data set as in Fig. 1(c)] at the actual measurement time; the color map for T_1 is the same as in Fig. 1. Note that the vertical axis is truncated at $t = 5$ h to display the relative measurement times more clearly.

APPENDIX C: EXPERIMENTAL DETAILS

The spectrotemporal charts displayed in Sec. IV can be interpreted as matrices of T_1 values, with m rows and n columns; m and n represent a time and frequency index, respectively. The (1,1) entry is the bottom-left element of the matrix, such that time increases from bottom to top. We set f_q from low to high values, completing one row of each matrix when reaching the highest value of f_q. Subsequent rows are measured restarting always from the lowest value of f_q. Hence, the time $t_{m,n}$ at which each data point (m, n) is taken increases from left to right for the mth row, starting at $t_{m,1}$ and ending at t_{m,N_f}. The time difference between subsequent rows is a constant value defined as $\Delta t = t_{m+1,1} - t_{m,1}$. Although each measurement in any particular row is taken at a different time, we choose to display the data on a rectangular matrix where each row element is associated with the same time value. As a comparison, Fig. 4 shows a scatter plot for which each T_1 value is plotted at the actual measurement time. This figure elucidates two limitations of our experiments: (1) The impossibility to measure an entire row at exactly the same time. (2) The fact that $t_{m,N_f} \sim t_{m+1,1}$. It additionally stresses a difference between experiments and simulations, i.e., the fact that in simulations all row elements are calculated at the exact same time.

In order to keep Δt constant, we must account for experimental nonidealities. The time required to perform a single T_1 experiment is $t_{\exp} \approx 16$ s and varies slightly between experiments. In addition, latencies in the electronic equipment

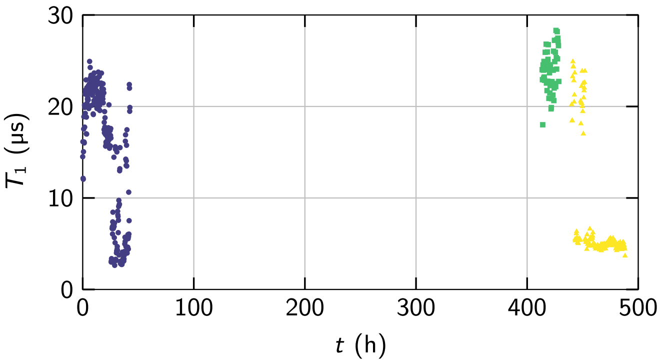

FIG. 5. Time series of T_1 vs t showing the relative time between measurements for data set 1 (blue dots) and 3 (yellow triangles) [same data sets as in Figs. 1(a) and 1(c)] and an additional data set (green squares); all data sets are for $f_q = 4.529$ GHz.

when setting a new value of f_q result in a short time overhead. To overcome these issues, we measure a test row and record the corresponding measurement time. We then augment this measurement time by a certain buffer time, which we estimate to be sufficiently longer than any possible time variations due to nonidealities. The sum of the measurement time of the test row and the buffer time is Δt. For example, for the data set shown in Fig. 1(c), the time elapsed to acquire the data of the test row is approximately 992 s. In this case, we choose $\Delta t = 1000$ s. The values of Δt for each data set shown in Sec. IV are reported in Table I.

APPENDIX D: LONG-TIME STABILITY

One of the assumptions in Sec. III is that the TLS parameters do not change in time, i.e., they are considered to be *static*. Thus, the only dynamically varying quantity is the state of a TLS. In order to show that this is a reasonable assumption, in Fig. 5 we display three experimental time series measured at $f_q = 4.529$ GHz. The first time series corresponds to a column extracted from the spectrotemporal chart of Fig. 1(a); the second series is an additional trace not included in the spectrotemporal charts because it is too short compared to the other traces; finally, the third series is a column from Fig. 1(c). Each point in the three series is plotted at the actual time at which it is measured relative to the first point of the first series. It is worth noting that the frequency of these time series is not captured in the spectrotemporal chart of Fig. 1(b).

The three time series are measured over the course of approximately three weeks. Despite the large time gap between the first and third series, we observe a similar T_1-drop pattern: the T_1 times are distributed around two values, 5 and 23 μs. These results indicate a reproducible feature and suggest a static TLS distribution.

It is well known that by cycling the sample temperature, e.g., when warming up and cooling back down a device, results in a strain field that can modify the TLS parameters. However, when operating a sample at a constant temperature and without exceedingly large excitation electric fields (as in the experiments reported in this work), we expect a static TLS distribution.

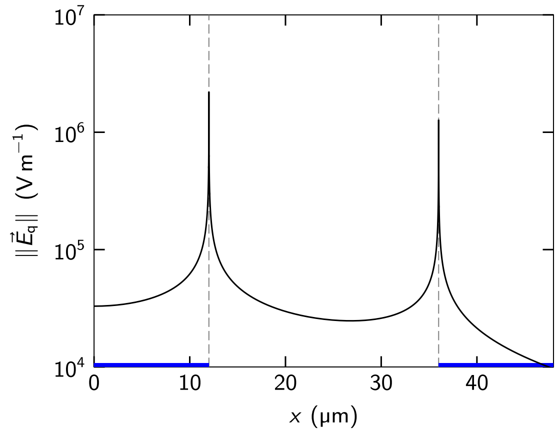

FIG. 6. Qubit electric field $||\vec{E}_q||$ for $\phi_0 = 1$ V vs width x at one value of the height $z = 1.5$ nm. The origin of the graph is at $x = 0$, corresponding to the middle point of the strip. Due to the symmetry of the CPW segment with respect to its longitudinal axis (i.e., the y axis; not shown), we display $||\vec{E}_q(x)||$ only for half of the CPW segment, for $x \geqslant 0$. The extent of the conducting sections of the CPW is indicated by the thick blue lines. The dashed black vertical lines are placed at the edge of each conductor; the left line corresponds to the edge of the strip and the right line to the edge of the ground plane.

APPENDIX E: QUBIT ELECTRIC FIELD

As explained in Appendix B, the qubit capacitor is a Greek cross formed by two CPW strips of length L. Since $L \gg S + W$, we approximate the qubit capacitor as a CPW segment of infinite length; we additionally assume that the capacitor is made of an infinitesimally thin conducting sheet. When determining $\vec{E}_q$, we can thus restrict ourselves to points within the CPW vertical cross section.

We determine $\vec{E}_q$ by means of a conformal mapping technique. A conformal map is a function that locally preserves angles, allowing us to transform the CPW geometry into that of a much simpler infinite parallel-plate capacitor; the map function is given by Eq. (25) in the work of Ref. [43]. We then use this map to transform the electric field of the parallel-plate capacitor into that of the CPW. The electric field is proportional to the qubit electric vacuum potential with respect to ground, or zero-point voltage; given the qubit plasma frequency $f_p = \sqrt{8E_J E_c}/h$, the zero-point voltage reads as

$$\phi_0 \simeq \sqrt{\frac{hf_p}{2C_q}} = \frac{e}{C_q}\left(\frac{E_J}{2E_c}\right)^{1/4} \sim 4\ \mu\text{V}. \qquad \text{(E1)}$$

In order to generate g, we evaluate $||\vec{E}_q||$ at randomly picked points (x, z) corresponding to Q-TLS positions. These points are confined within the cross-section region introduced above. The cross section is centered on the middle point of the strip and has a length of 96 μm and a height of 3 nm; the left and right edges of the cross section extend 12 μm into the ground plane and the top edge corresponds to the oxide layer's top edge. Figure 6 shows $||\vec{E}_q(x, z)||$.

[1] M. Kjaergaard, M. E. Schwartz, J. Braumüller, P. Krantz, J. I.-J. Wang, S. Gustavsson, and W. D. Oliver, Superconducting qubits: Current state of play, Annu. Rev. Condens. Matter Phys. **11**, 369 (2020).

[2] C. Müller, J. H. Cole, and J. Lisenfeld, Towards understanding two-level-systems in amorphous solids: insights from quantum circuits, Rep. Prog. Phys. **82**, 124501 (2019).

[3] W. A. Phillips, Two-level states in glasses, Rep. Prog. Phys. **50**, 1657 (1987).

[4] C. T. Earnest, J. H. Béjanin, T. G. McConkey, E. A. Peters, A. Korinek, H. Yuan, and M. Mariantoni, Substrate surface engineering for high-quality silicon/aluminum superconducting resonators, Supercond. Sci. Technol. **31**, 125013 (2018).

[5] J. H. Béjanin, C. T. Earnest, Y. R. Sanders, and M. Mariantoni, Resonant coupling parameter estimation with superconducting qubits, arXiv:2008.12714.

[6] L. Frunzio, A. Wallraff, D. Schuster, J. Majer, and R. Schoelkopf, Fabrication and characterization of superconducting circuit QED devices for quantum computation, IEEE Trans. Appl. Supercond. **15**, 860 (2005).

[7] R. Barends, J. Kelly, A. Megrant, D. Sank, E. Jeffrey, Y. Chen, Y. Yin, B. Chiaro, J. Mutus, C. Neill, P. O'Malley, P. Roushan, J. Wenner, T. C. White, A. N. Cleland, and J. M. Martinis, Coherent Josephson Qubit Suitable for Scalable Quantum Integrated Circuits, Phys. Rev. Lett. **111**, 080502 (2013).

[8] J. M. Martinis, K. B. Cooper, R. McDermott, M. Steffen, M. Ansmann, K. D. Osborn, K. Cicak, S. Oh, D. P. Pappas, R. W. Simmonds, and C. C. Yu, Decoherence in Josephson Qubits from Dielectric Loss, Phys. Rev. Lett. **95**, 210503 (2005).

[9] J. Gao, M. Daal, J. M. Martinis, A. Vayonakis, J. Zmuidzinas, B. Sadoulet, B. A. Mazin, P. K. Day, and H. G. Leduc, A semiempirical model for two-level system noise in superconducting microresonators, Appl. Phys. Lett. **92**, 212504 (2008).

[10] D. S. Wisbey, J. Gao, M. R. Vissers, F. C. S. da Silva, J. S. Kline, L. Vale, and D. P. Pappas, Effect of metal/substrate interfaces on radio-frequency loss in superconducting coplanar waveguides, J. Appl. Phys. **108**, 093918 (2010).

[11] J. M. Sage, V. Bolkhovsky, W. D. Oliver, B. Turek, and P. B. Welander, Study of loss in superconducting coplanar waveguide resonators, J. Appl. Phys. **109**, 063915 (2011).

[12] A. Megrant, C. Neill, R. Barends, B. Chiaro, Y. Chen, L. Feigl, J. Kelly, E. Lucero, M. Mariantoni, P. J. J. O'Malley, D. Sank, A. Vainsencher, J. Wenner, T. C. White, Y. Yin, J. Zhao, C. J. Palmstrøm, J. M. Martinis, and A. N. Cleland, Planar superconducting resonators with internal quality factors above one million, Appl. Phys. Lett. **100**, 113510 (2012).

[13] C. J. K. Richardson, N. P. Siwak, J. Hackley, Z. K. Keane, J. E. Robinson, B. Arey, I. Arslan, and B. S. Palmer, Fabrication artifacts and parallel loss channels in metamorphic epitaxial aluminum superconducting resonators, Supercond. Sci. Technol. **29**, 064003 (2016).

[14] A. Dunsworth, A. Megrant, C. Quintana, Z. Chen, R. Barends, B. Burkett, B. Foxen, Y. Chen, B. Chiaro, A. Fowler, R. Graff, E. Jeffrey, J. Kelly, E. Lucero, J. Y. Mutus, M. Neeley, C. Neill, P. Roushan, D. Sank, A. Vainsencher *et al.*, Characterization and reduction of capacitive loss induced by sub-micron josephson junction fabrication in superconducting qubits, Appl. Phys. Lett. **111**, 022601 (2017).

[15] S. E. de Graaf, L. Faoro, J. Burnett, A. A. Adamyan, A. Ya. Tzalenchuk, S. E. Kubatkin, T. Lindström, and A. V. Danilov, Suppression of low-frequency charge noise in superconducting resonators by surface spin desorption, Nat. Commun. **9**, 1143 (2018).

[16] M. Moeed, C. Earnest, J. Béjanin, A. Sharafeldin, and M. Mariantoni, Improving the time stability of superconducting planar resonators, MRS Adv. **4**, 2201 (2019).

[17] A. Bilmes, S. Volosheniuk, J. D. Brehm, A. V. Ustinov, and J. Lisenfeld, Quantum sensors for microscopic tunneling systems, npj Quantum Inf. **7**, 27 (2021).

[18] J. Wenner, R. Barends, R. C. Bialczak, Y. Chen, J. Kelly, E. Lucero, M. Mariantoni, A. Megrant, P. J. J. O'Malley, D. Sank, A. Vainsencher, H. Wang, T. C. White, Y. Yin, J. Zhao, A. N. Cleland, and J. M. Martinis, Surface loss simulations of superconducting coplanar waveguide resonators, Appl. Phys. Lett. **99**, 113513 (2011).

[19] J. M. Gambetta, C. E. Murray, Y. K. K. Fung, D. T. McClure, O. Dial, W. Shanks, J. W. Sleight, and M. Steffen, Investigating surface loss effects in superconducting transmon qubits, IEEE Trans. Appl. Supercond. **27**, 1 (2017).

[20] W. Woods, G. Calusine, A. Melville, A. Sevi, E. Golden, D. K. Kim, D. Rosenberg, J. L. Yoder, and W. D. Oliver, Determining Interface Dielectric Losses in Superconducting Coplanar-Waveguide Resonators, Phys. Rev. Appl. **12**, 014012 (2019).

[21] M. Neeley, M. Ansmann, R. C. Bialczak, M. Hofheinz, N. Katz, E. Lucero, A. O'Connell, H. Wang, A. N. Cleland, and J. M. Martinis, Process tomography of quantum memory in a josephson-phase qubit coupled to a two-level state, Nat. Phys. **4**, 523 (2008).

[22] J. Burnett, L. Faoro, I. Wisby, V. L. Gurtovoi, A. V. Chernykh, G. M. Mikhailov, V. A. Tulin, R. Shaikhaidarov, V. Antonov, P. J. Meeson, A. Ya. Tzalenchuk, and T. Lindström, Evidence for interacting two-level systems from the 1/f noise of a superconducting resonator, Nat. Commun. **5**, 4119 (2014).

[23] L. Faoro and L. B. Ioffe, Interacting tunneling model for two-level systems in amorphous materials and its predictions for their dephasing and noise in superconducting microresonators, Phys. Rev. B **91**, 014201 (2015).

[24] C. Müller, J. Lisenfeld, A. Shnirman, and S. Poletto, Interacting two-level defects as sources of fluctuating high-frequency noise in superconducting circuits, Phys. Rev. B **92**, 035442 (2015).

[25] C. Neill, A. Megrant, R. Barends, Y. Chen, B. Chiaro, J. Kelly, J. Y. Mutus, P. J. J. O'Malley, D. Sank, J. Wenner, T. C. White, Y. Yin, A. N. Cleland, and J. M. Martinis, Fluctuations from edge defects in superconducting resonators, Appl. Phys. Lett. **103**, 072601 (2013).

[26] H. Paik, D. I. Schuster, L. S. Bishop, G. Kirchmair, G. Catelani, A. P. Sears, B. R. Johnson, M. J. Reagor, L. Frunzio, L. I. Glazman, S. M. Girvin, M. H. Devoret, and R. J. Schoelkopf, Observation of High Coherence in Josephson Junction Qubits Measured in a Three-Dimensional Circuit QED Architecture, Phys. Rev. Lett. **107**, 240501 (2011).

[27] J. J. Burnett, A. Bengtsson, M. Scigliuzzo, D. Niepce, M. Kudra, P. Delsing, and J. Bylander, Decoherence benchmarking of superconducting qubits, npj Quantum Inf. **5**, 54 (2019).

[28] S. Schlör, J. Lisenfeld, C. Müller, A. Bilmes, A. Schneider, D. P. Pappas, A. V. Ustinov, and M. Weides, Correlating Decoherence in Transmon Qubits: Low Frequency Noise by Single Fluctuators, Phys. Rev. Lett. **123**, 190502 (2019).

[29] M. Carroll, S. Rosenblatt, P. Jurcevic, I. Lauer, and A. Kandala, Dynamics of superconducting qubit relaxation times, arXiv:2105.15201.

[30] P. V. Klimov, J. Kelly, Z. Chen, M. Neeley, A. Megrant, B. Burkett, R. Barends, K. Arya, B. Chiaro, Y. Chen, A. Dunsworth, A. Fowler, B. Foxen, C. Gidney, M. Giustina, R. Graff, T. Huang, E. Jeffrey, E. Lucero, J. Y. Mutus *et al.*, Fluctuations of Energy-Relaxation Times in Superconducting Qubits, Phys. Rev. Lett. **121**, 090502 (2018).

[31] P. Esquinazi, *Tunneling Systems in Amorphous and Crystalline Solids* (Springer, Berlin, 1998).

[32] J. Lisenfeld, C. Müller, J. H. Cole, P. Bushev, A. Lukashenko, A. Shnirman, and A. V. Ustinov, Measuring the Temperature Dependence of Individual Two-Level Systems by Direct Coherent Control, Phys. Rev. Lett. **105**, 230504 (2010).

[33] A. Kamal, J. L. Yoder, F. Yan, T. J. Gudmundsen, D. Hover, A. P. Sears, P. Welander, T. P. Orlando, S. Gustavsson, and W. D. Oliver, Improved superconducting qubit coherence with high-temperature substrate annealing, arXiv:1606.09262.

[34] C. R. H. McRae, J. H. Béjanin, C. T. Earnest, T. G. McConkey, J. R. Rinehart, C. Deimert, J. P. Thomas, Z. R. Wasilewski, and M. Mariantoni, Thin film metrology and microwave loss characterization of indium and aluminum/indium superconducting planar resonators, J. Appl. Phys. **123**, 205304 (2018).

[35] J. Bezanson, A. Edelman, S. Karpinski, and V. B. Shah, Julia: A fresh approach to numerical computing, SIAM Rev. **59**, 65 (2017).

[36] J. Béjanin, QubitFluctuations.jl, https://gitlab.com/DQMLab/qubitfluctuations.

[37] A. F. Wells, *Structural Inorganic Chemistry*, 5th ed. (Clarendon, Oxford, 1984).

[38] T. T. Song, M. Yang, J. W. Chai, M. Callsen, J. Zhou, T. Yang, Z. Zhang, J. S. Pan, D. Z. Chi, Y. P. Feng, and S. J. Wang, The stability of aluminium oxide monolayer and its interface with two-dimensional materials, Sci. Rep. **6**, 29221 (2016).

[39] H. J. Mamin, E. Huang, S. Carnevale, C. T. Rettner, N. Arellano, M. H. Sherwood, C. Kurter, B. Trimm, M. Sandberg, R. M. Shelby, M. A. Mueed, B. A. Madon, A. Pushp, M. Steffen, and D. Rugar, Merged-Element Transmons: Design and Qubit Performance, Phys. Rev. Appl. **16**, 024023 (2021).

[40] W. Riley, *Handbook of Frequency Stability Analysis* (NIST, Gaithersburg, MD, 2008).

[41] Y. Chu, P. Kharel, T. Yoon, L. Frunzio, P. T. Rakich, and R. J. Schoelkopf, Creation and control of multi-phonon Fock states in a bulk acoustic-wave resonator, Nature (London) **563**, 666 (2018).

[42] P. Meystre and M. Sargent, *Elements of Quantum Optics*, 4th ed. (Springer, Berlin, 2007).

[43] C. E. Murray, J. M. Gambetta, D. T. McClure, and M. Steffen, Analytical determination of participation in superconducting coplanar architectures, IEEE Trans. Microwave Theory Technol. **66**, 3724 (2018).